Blood flow dynamics and fluid–structure interaction in patient-specific bifurcating cerebral aneurysms

Alvaro Valencia[1,*,†], Darren Ledermann[1], Rodrigo Rivera[2], Eduardo Bravo[2] and Marcelo Galvez[2]

[1]*Department of Mechanical Engineering, Universidad de Chile, Casilla 2777, Santiago, Chile*
[2]*Neuroradiology Department, Instituto de Neurocirugía Asenjo, Jose Manuel Infante 553, Santiago, Chile*

SUMMARY

Hemodynamics plays an important role in the progression and rupture of cerebral aneurysms. The current work describes the blood flow dynamics and fluid–structure interaction in seven patient-specific models of bifurcating cerebral aneurysms located in the anterior and posterior circulation regions of the circle of Willis. The models were obtained from 3D rotational angiography image data, and blood flow dynamics and fluid–structure interaction were studied under physiologically representative waveform of inflow. The arterial wall was assumed to be elastic, isotropic and homogeneous. The flow was assumed to be laminar, non-Newtonian and incompressible. In one case, the effects of different model suppositions and boundary conditions were reported in detail. The fully coupled fluid and structure models were solved with the finite elements package ADINA. The vortex structure, pressure, wall shear stress (WSS), effective stress and displacement of the aneurysm wall showed large variations, depending on the morphology of the artery, aneurysm size and position. The time-averaged WSS, effective stress and displacement at the aneurysm fundus vary between 0.17 and 4.86 Pa, 4.35 and 170.2 kPa and 0.16 and 0.74 mm, respectively, for the seven patient-specific models of bifurcating cerebral aneurysms.

KEY WORDS: cerebral aneurysm; wall shear stress; effective wall stress; displacement; 3D rotational X-ray angiography

*Correspondence to: Alvaro Valencia, Department of Mechanical Engineering, Universidad de Chile, Casilla 2777, Santiago, Chile.
†E-mail: alvalenc@ing.uchile.cl, alvalenc@cec.uchile.cl

Contract/grant sponsor: FONDECYT Chile; contract/grant number: 1070773

1. INTRODUCTION

Cerebral aneurysms are pathologic dilations of an artery, generally found in the anterior and posterior regions of the circle of Willis. Rupture of a cerebral aneurysm causes subarachnoid hemorrhage (SAH) with potentially severe neurologic complications [1]. The SAH is a bleeding into the area between the arachnoid membrane and the pia mater of the brain. Cerebral aneurysms can be classified into terminal, lateral or bifurcation aneurysms depending on their relationship with the parent artery. Typically, cerebral aneurysms arise at a bifurcation or along a curve of the parent vessel. Classic treatments of cerebral aneurysms are direct surgical clipping or endovascular coil insertion. The coils promote blood coagulation inside the aneurysm, thereby avoiding blood flow and thus excluding the aneurysm from the circulation [1].

A typical cerebral aneurysm wall has a very thin tunica media or none, and the internal elastic lamina is either absent or severely fragmented. Thus, the aneurysm wall is generally composed of only intima and adventitia [1]. The aneurysm wall, which must withstand arterial blood pressure, is composed of layered collagen. Wall strength is related to both collagen fiber strength and orientation. Average breaking strength of the aneurysm wall ranging from 0.73 to 1.9 MPa has been estimated [2]. Fluid shear stress modulates endothelial cell remodeling via realignment and elongation, and the time variation of wall shear stress (WSS) significantly affects the rates at which endothelial cells are remodeled [3]. Consequently, hemodynamic factors, such as blood velocity, WSS, pressure, particle residence time and flow impingement, play important roles in the growth and rupture of cerebral aneurysms.

Several authors have reported the importance of WSS on the development, growth and rupture of cerebral aneurysms [4–6]. High WSS is regarded as a major factor in the development and growth of cerebral aneurysms [4]. Aneurysm rupture is related to a low level of WSS; therefore, it is associated with low-flow conditions [5]. The aneurysm region with low-flow conditions is normally the aneurysm fundus, i.e. the dome region of the aneurysm. The WSS is converted into biological signals via mechanoreceptors on endothelial cells, and it modules the cellular functions of the artery wall. The mechanoreceptors are sensory receptors that respond to artery pressure. It is assumed that a WSS of approximately 2 Pa is suitable for maintaining the structure of the aneurysm wall, whereas a lower WSS results in the degeneration of endothelial cells via the apoptotic cell cycle [7]. An apoptotic cell cycle is a form of programmed cell death that involves complex biochemical processes. For this reason, studies of blood flow dynamics inside models of cerebral aneurysms are important to obtain quantitative criteria to determinate the rupture risk of aneurysms.

Steinman *et al.* [8] reported image-based computational simulations of the flow dynamics (CFD) for Newtonian fluid in a giant cerebral aneurysm. CFD analysis revealed high-velocity flow entering the aneurysm at the proximal and distal ends of the neck, promoting the formation of both persistent and transient vortices within the aneurysm sac. Cebral *et al.* [9] described a clinical study in which the association between intra-aneurysmal hemodynamic characteristics from CFD models and the rupture of cerebral aneurysms was investigated. A total of 62 patient-specific models of cerebral aneurysms were constructed from 3D angiography images. The aneurysms were classified into different categories depending on the complexity and stability of the flow pattern, the location and the size of the flow impingement region, and the size of the inflow jet. Cebral *et al.* [10] presented a sensitivity analysis of the hemodynamic characteristics with respect to variations involving several variables in patient-specific models of cerebral aneurysms; they found that the variable that had the greatest effect on the flow field was the vessel geometry.

Shojima *et al.* [5] simulated blood flow in 20 patient-specific cerebral aneurysms located in the middle cerebral artery; the calculated WSS on the aneurysm fundus was significantly lower than the WSS on the surrounding vasculature. Further, they found an inverse linear relationship between the aneurysm aspect ratio and the WSS on the aneurysm fundus at peak systole. Hassan *et al.* [11] using CFD in 68 patient-specific cerebral aneurysm models have proposed linear correlations between the aneurysm neck and the aneurysm depth, and between the diameter of the draining artery and the aneurysm depth, respectively. Ma *et al*. [12] have performed a 3D geometrical characterization of human cerebral aneurysms from computed tomogram angiography data. This geometry can be classified as hemispheric, ellipsoidal or spherical; it is apparent that aneurysm shape is more effective than size in discriminating between ruptured and unruptured aneurysms. Valencia *et al.* [13] describe the blood flow dynamics in 34 patient-specific models of saccular aneurysms located in the region of the anterior and posterior circulation of the circle of Willis. They have found a correlation between the mean WSS on the aneurysmal sac for unruptured lateral and ruptured lateral aneurysms with an aneurysm surface index, which is defined as the ratio of the aneurysm area to the artery area at the model inlet.

The influence of the non-Newtonian properties of blood in a patient-specific model of carotid artery with a saccular aneurysm was investigated in detail by Valencia *et al.* [14]. The effect of the non-Newtonian properties of blood on WSS was important only in the arterial regions with high-velocity gradient; on the aneurysm wall, the predictions with the Newtonian and non-Newtonian blood models were similar. The effect of arterial compliance has been considered in few reported studies of hemodynamics in patient-specific cerebral aneurysm models. The influence of wall elasticity has been reported in [15, 16]; it was shown that the effects of wall elasticity on WSS depend on arterial geometry. In bifurcating aneurysm models, the effects were more important than in lateral aneurysm models, and the differences in WSS between the model with elastic walls and the model with rigid walls can reach up to 50%.

Another hypothesis about the mechanism of aneurysm rupture is based on progressive wall remodeling under the effect of pulsatile blood pressure. The time periodic resulting tensional effective wall stress and deformation play an important role in wall remodeling, and the mechanism of rupture could be based on plastic deformation under fatigue-like mechanism. Wall strength is related to both collagen fiber strength and orientation in the aneurysm wall [2].

In the current work, we present detailed numerical simulations of hemodynamics including fluid–structure interaction (FSI) in seven bifurcating cerebral aneurysm models. The aneurysms were located in different cerebral arteries and reconstructed from 3D rotational angiography image data. The purpose of this study is to report the different flow characteristics: pressure, WSS, wall deformation and effective wall stress of each bifurcating cerebral aneurysm. This study included three unruptured and four ruptured bifurcating cerebral aneurysms (Figure 1). This investigation provides valuable insight into the hemodynamics and the related wall stress in cerebral aneurysms subject to physiologically realistic pulsatile loads. The effects of inlet fluid boundary condition, fluid model and Young's modulus were reported for case 1. Also the results on wall stress and deformation considering only the solid model were reported and compared with the corresponding CFD with FSI results in case 1.

In addition, pre-procedural planning for cerebral aneurysm endovascular treatments will benefit from an accurate assessment of flow patterns and effective wall stress in the aneurysm as presented in this work by means of CFD including FSI. The goal of this work is to relate aneurysm state

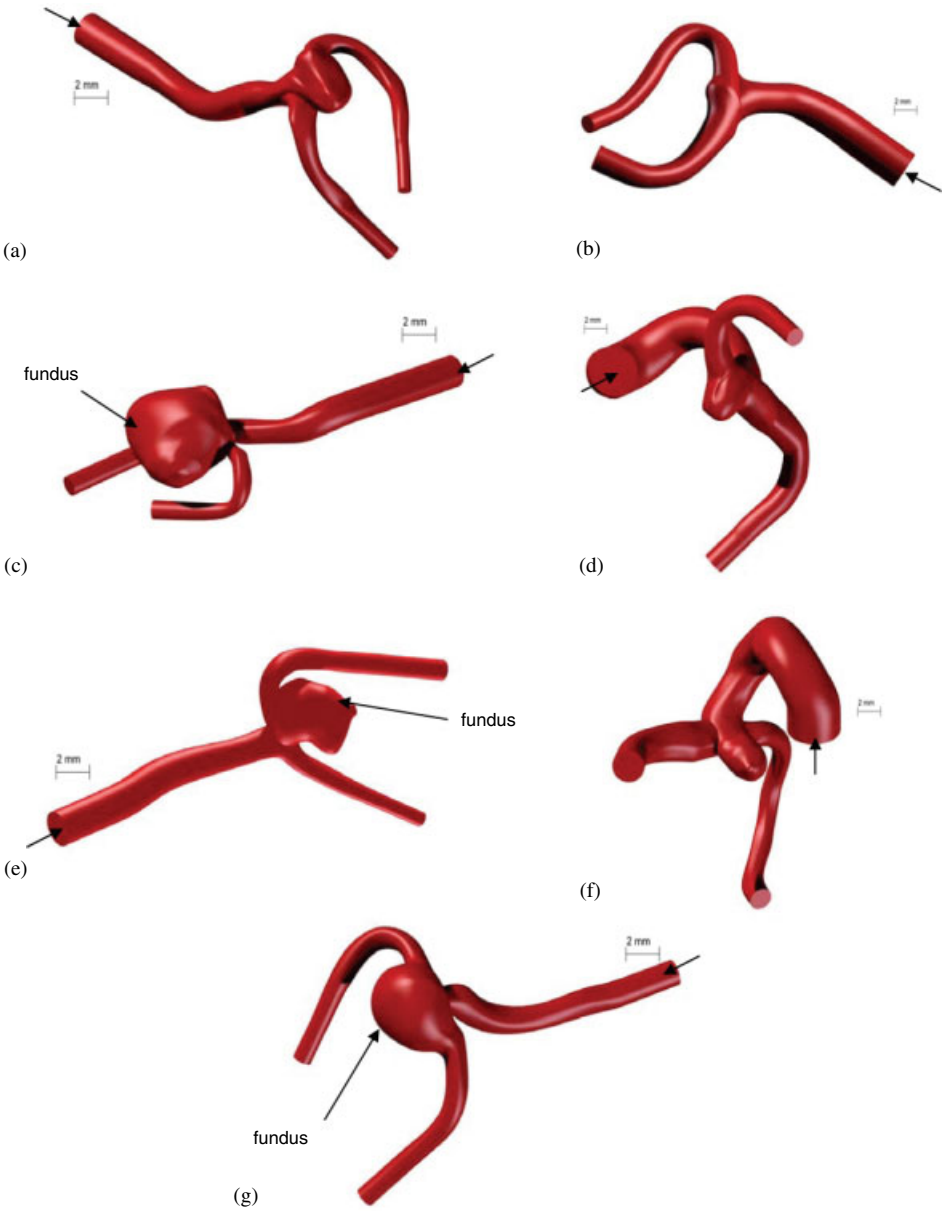

Figure 1. Patient-specific models of bifurcating cerebral aneurysms. (a) (Case 1), (c) (case 3), (e) (case 5), (g) (case 7): ruptured middle cerebral; (b) case 2: unruptured ophthalmic segment; and (d) (case 4), (f) (case 6): unruptured posterior communicating.

(unruptured or ruptured) with WSS, wall deformation and effective wall stress; such a relationship would provide information for the diagnosis and treatment of unruptured and ruptured aneurysms by elucidating the risk of bleeding or rebleeding, respectively.

2. METHODS

2.1. Reconstruction methodology

Cerebral angiography rotational acquisitions were obtained by using a Phillips Integris Allura system. The images were obtained during a 180° rotation with imaging at 30 frames/s. The corresponding 100 projection images were reconstructed into a 3D data set using an isotropic voxel on a dedicated Phillips workstation. The Allura 3DRA technology includes complete vascular coverage in 3D with a resolution greater than 12 pixels/mm, and the pixel thresholds are adjusted automatically. The file in VRML format was exported to the 3DSMax software for cleaning and exported in STL format to 3D-Doctor software. The parameterization of the contours was made using the software 3D-Doctor from different cut planes using B-spline. Contours were obtained and exported in IGES format to the computer-aided design (CAD) Rhinoceros software. In Rhinoceros, non-uniform, rational B-spline surfaces (NURBS) were generated, and the different surfaces were pasted to create the 3D geometry of the arteries with cerebral aneurysm. Finally, the geometry was exported from Rhinoceros in Parasolid format to the finite element package ADINA v8.3 [17]. An unstructured grid was generated in the fluid domain using tetrahedral elements with four nodes. This reconstruction method is fast and the influence of the operator on the final geometry is minimal [13].

Four bifurcating aneurysms with previous rupture of the middle cerebral artery and three unruptured bifurcating aneurysms of different arteries were reconstructed as shown in Figure 1. Table I shows the principal geometrical characteristics of the seven cases such as aneurysm area and aneurysm volume. The volume of the three unruptured aneurysms (cases 2, 4 and 6) is lower than the corresponding volume of the four ruptured aneurysms (cases 1, 3, 5 and 7). The aneurysm surface index R_1, which is defined as the ratio of the aneurysm area to the artery area at the model inlet, is also shown in Table I [13].

2.2. Governing equations for FSI

For the fluid model, the flow was assumed to be laminar, non-Newtonian and incompressible. The incompressible Navier–Stokes equations with arbitrary Lagrangian–Eulerian (ALE) formulation were used as the governing equations that are suitable for problems with FSI and frequent mesh adjustments. Flow velocity at the flow–artery interface was set to move with the artery wall. The

Table I. Geometrical characteristics.

Case	A (mm^2)	A_i (mm^2)	$R_1 = A/A_i$	V (mm^3)	V_T (mm^3)
1	64.08	5.632	11.4	88.60	247.1
2	25.39	9.292	2.7	5.75	300.0
3	243.18	6.005	40.5	321.42	500.4
4	70.65	15.606	4.5	43.85	572.6
5	139.93	7.488	18.7	126.28	354.5
6	62.16	19.977	3.1	39.80	617.8
7	169.17	4.023	42.1	187.81	386.0

A, aneurysm area; A_i, artery area at the inlet of computational domain; R_1, aneurysm surface index [13]; V, aneurysm volume; V_T, geometric volume.

mass and momentum conservation equations for an incompressible fluid can be expressed as

$$\nabla \cdot \mathbf{u} = 0 \tag{1}$$

$$\rho_{\mathrm{f}}(\partial \mathbf{u}/\partial t + ((\mathbf{u}-\mathbf{u}_g)\cdot\nabla)\mathbf{u}) = -\nabla p + \nabla \cdot \boldsymbol{\tau} \tag{2}$$

where ρ_{f} is the fluid density, p is the pressure, $\mathbf{u}$ is the fluid velocity vector and $\mathbf{u}_g$ is the moving coordinate velocity. In the ALE formulation, $(\mathbf{u}-\mathbf{u}_g)$ is the relative velocity of the fluid with respect to the moving coordinate velocity. Here $\boldsymbol{\tau}$ is the deviatoric stress tensor. This tensor is related to the strain rate tensor; however, this relationship is usually expressed as an algebraic equation of the form

$$\boldsymbol{\tau} = \mu \dot{\gamma}_{ij} \tag{3}$$

where μ is the viscosity and $\dot{\gamma}_{ij}$ is the strain rate, which is defined for an incompressible fluid as

$$\dot{\gamma}_{ij} = \left(\frac{\partial v_i}{\partial x_j} + \frac{\partial v_j}{\partial x_i} \right) \tag{4}$$

Blood is a suspension of red blood cells in plasma. The viscosity of blood is mainly dependent on the volume fraction of red blood cells in the plasma. We considered the effects of a non-Newtonian fluid model on hemodynamics. The Carreau fluid model was selected because it is an accurate model to describe the rheological behavior of blood [18]. The Carreau fluid model of blood assumes that the viscosity, μ, varies according to the law

$$\mu = \mu_\infty + (\mu_0 - \mu_\infty)\cdot(1 + K\dot{\gamma}_{ij}^2)^n \tag{5}$$

The Carreau blood model predicts decreasing viscosity at high strain, where μ_0 and μ_∞ are low and high shear rate asymptotic values, and parameters K and n control the transition region. Parameter μ_∞ can be obtained with the same method used for viscosity in a Newtonian fluid model. We have taken the experimental values recommended in [18] as $\mu_\infty = 0.00345\,\mathrm{Ns/m^2}$, $\mu_0 = 0.056\,\mathrm{Ns/m^2}$, $K = 10.976$ and $n = -0.3216$. The density of blood was assumed to be constant, $\rho = 1050\,\mathrm{kg/m^3}$.

The governing equation for the solid domain is the momentum conservation equation given by Equation (6). In contrast to the ALE formulation of the fluid equations, a Lagrangian coordinate system is adopted:

$$\nabla \cdot \boldsymbol{\sigma}_{\mathrm{s}} = \rho_{\mathrm{s}} \dot{\mathbf{u}}_g \tag{6}$$

where ρ_{s} is the solid density, $\boldsymbol{\sigma}_{\mathrm{s}}$ is the solid stress tensor and $\dot{\mathbf{u}}_g$ is the local acceleration of the solid. The FSI interface states that (i) displacements of the fluid and solid domain must be compatible; (ii) tractions at this boundary must be at equilibrium and (iii) fluid must obey the no-slip condition. These conditions are given in the following equations:

$$\boldsymbol{\delta}_{\mathrm{s}} = \boldsymbol{\delta}_{\mathrm{f}} \tag{7}$$

$$\boldsymbol{\sigma}_{\mathrm{s}} \cdot \hat{\mathbf{n}}_{\mathrm{s}} = \boldsymbol{\sigma}_{\mathrm{f}} \cdot \hat{\mathbf{n}}_{\mathrm{f}} \tag{8}$$

$$\mathbf{u} = \mathbf{u}_g \tag{9}$$

where $\boldsymbol{\delta}, \boldsymbol{\sigma}$ and $\hat{\mathbf{n}}$ are, respectively, displacement, stress tensor and boundary normal with the subscripts 'f' and 's' indicating a property of the fluid and solid, respectively. The condition of

DOI: 10.1002/fld

Equation (8) does not require identical matching meshes between the two domains but instead supports the use of solution mapping to establish the equilibrium [19]. An external boundary condition of pressure is also applied:

$$(\boldsymbol{\sigma}_s \hat{\mathbf{n}}_s) \cdot \hat{\mathbf{n}}_s = P_c \tag{10}$$

where P_c is the intracranial pressure produced by the cerebral spinal fluid and it was assumed to be constant, $P_c = 400\,\text{Pa}$ [20].

The artery wall was assumed as isotropic, incompressible and homogeneous with density $\rho_s = 1050\,\text{kg/m}^3$ [20] and Poisson's ratio $\upsilon = 0.45$ [15]. The average wall thickness of cerebral aneurysms measured in [2, 21] are 0.11 and 0.086 mm, respectively. Cerebral aneurysms exhibit a nonlinear response over finite strains that is typical for soft biological tissues [21]; however, for pressure of 100 mmHg the aneurysm wall stretch ratio is only around 1.05 [21]. Based on this information, the aneurysm wall was modeled in this work as an elastic shell with an elastic modulus $E = 2\,\text{MPa}$; the value of E was obtained as the slope of the curve stress *versus* stretch for specimen S_1 in Figure 4(a) of [21]. Similar values of elastic modulus, $E = 1.6\,\text{MPa}$, for intracranial arteries are considered in [22].

2.3. Boundary conditions for the fluid and solid domain

Physiological flow conditions were imposed at the inlet using flow measurements with pulsed Doppler ultrasound acquired from the extracranial right internal carotid artery in each patient. Figure 2(a) shows the time dependence of the mean blood velocity in each patient. The large variation in velocity in each patient shows the importance of considering patient-specific velocity profile; the heart rate was set as 70 beats per minute for the seven cases. The heart rate was not patient specific, because this measure was not available in the medical protocol of patients with aneurysms in this study, and the use of the same heart rate for the seven cases eliminates one variable of the problem. The time dependency of the inflow mean velocity $U(t)$ was represented by a Fourier series of order 15 for each patient:

$$U(t) = U_0 + \sum_{n=1}^{15} (a_n \cos(n\omega t) + b_n \sin(n\omega t)) \tag{11}$$

The maximal peak Reynolds number at systole is $Re_{\max} = 1560$ for case 6; this Reynolds number is lower than 2300, so that the flow can be considered laminar at the inlet.

The Womersley solution for the velocity profile in a straight pipe is used at the inlet for the variation of velocity profile with time and position:

$$u(r,t) = 2U_0 \left(1 - \left(\frac{r}{R}\right)^2\right) + \sum_{i=1}^{15} U_i \Re \left[\lambda \left[\frac{J_0(\lambda) - J_0\left(\lambda \frac{r}{R}\right)}{\lambda J_0(\lambda) - 2J_1(\lambda)} \right] \right] \tag{12}$$

where J_0 and J_1 are the Bessel functions of the first kind of order zero and one, respectively, R is the radius of the artery at the model inlet, $\lambda = ((i-1)/\sqrt{2})\alpha$, the function $\Re[]$ calculates the real part of a complex function and $\alpha = R\sqrt{\rho\omega/\mu}$ is the Womersley number [23]. The Womersley number, which depends on flow frequency $f = \omega/2\pi$, size of the artery and fluid viscosity, varied in each case. The Womersley number, which is used to measure the ratio of transient inertia

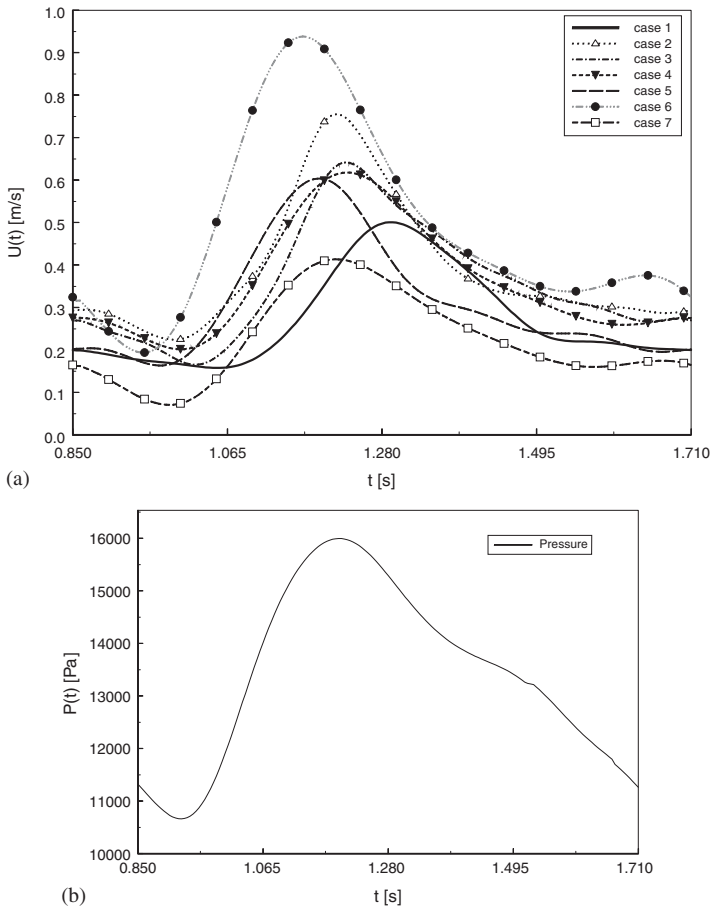

Figure 2. (a) Patient-specific waveform of the mean inlet velocity and (b) variation of pressure with time used as outlet boundary condition.

from pulsatility over viscous, varies between 1.8 (case 7) and 4.0 (case 6) in the pulsatile flow simulations. Two consecutive flow cycles were considered for the simulations.

The outflow boundary condition was defined with a pressure $P(t)$ at the exit of each cerebral artery. The time variation of pressure at the outlet ranged from 80 to 120 mmHg, see Figure 2(b), to obtain physiologically realistic pressure variations in the computational domain. The time dependency of outflow pressure $P(t)$ was represented by a Fourier series of order 5 [20]. Direct *in vivo* measure of pressure variation in intracranial arteries is impossible, and extracranial carotid artery pressure measurement was not included in the medical protocol of the patients.

Normally, the outflow boundary conditions for blood flow simulations are prescribed constant pressure and velocity profiles. Alternative approaches have been developed for the treatment of outflow boundary conditions, and they can be considered in future simulations. Using a 1D model, the flow rate and pressure can be related as a function of artery compliance and flow resistance [22]. However, due to lack of information about patient-specific artery compliance, this model

is general. The numerical treatment for outflow boundary conditions applied to arterial flow is described in detail in [24]. Outflow boundary conditions based on the Dirichlet-to-Neumann and variational multiscale methods for blood flow in arteries are proposed in [25]. Finally, the coupling of 3D and 1D Navier–Stokes equations for blood flow simulation in compliant arteries is showed in [26]. The artery compliance $C = \mathrm{d}A/\mathrm{d}P$ was not considered for the determination of exit pressure; the compliance can be approximated as $C = 3A_i R/2Eh$ [27], and for small cerebral arteries this effect can be neglected as first approximation.

For the solid model, the translations were restricted at artery inlet and at arteries outflows. These restrictions are applied far from the cerebral aneurysm; therefore, they do not affect the deformation and effective stress distributions in and around the aneurysm surface.

2.4. Numerical method

The fully coupled fluid and structure models were solved by a commercial finite element package ADINA (v8.3, ADINA R&D, Inc., Cambridge, MA), which has been tested by several applications [17, 19]. The finite element method (FEM) is used to solve the governing equations. The FEM discretizes the computational domain into finite elements that are interconnected by element nodal points. The fluid domain employs special flow-condition-based interpolation tetrahedral elements [17]. We have used the formulation with large displacements and small strains in the FSI calculation available in ADINA. The unstructured grids were composed of tetrahedral elements with four-node elements in the fluid and four-node isoparametric elements in the shell structure of the solid. As iteration, we used full Newton method with 172 time iterations using a time step of $\Delta t = 0.01$ s. A sparse matrix solver based on Gaussian elimination is used for solving the system. The relative tolerance for all degrees of freedom was set to 0.001.

To verify grid independence, numerical simulations based on the aneurysm model with rigid walls for case 1 were performed on seven grid sizes in the fluid. Table II shows the convergence of maximal pressure and cell Reynolds number in the computational domain at systole. Between the two finer grid sizes, the difference in predictions of maximal pressure and cell Reynolds number is only 0.7 and 1.8%, respectively. Considering that computational time increases linearly with grid size, we used a grid density of approximately 560 elements/mm^3 to determine the elements number of the grids used in the seven models of cerebral aneurysms. The workstation used to perform the simulations in this work is based on an Intel Xeon dual core 64 bits processor of 3.0 GHz clock speed with 8.0 GB RAM memory and runs on Linux CentOS 4.4 operating system.

Table II. Mesh refinement comparisons of maximal pressure and cell Reynolds number at systole for case 1.

Elements number	$P_{\max}$ (Pa)	Cell $Re \times 10^3$	Error at systole of cell Re %	Grid density (elements/mm^3)
58 218	31 815.4	61.36	86.4	235.6
63 338	30 055.5	53.51	62.6	276.5
74 423	29 836.7	49.96	51.8	301.2
102 876	27 391.5	38.27	16.3	416.3
123 250	26 586.0	34.65	5.3	498.8
139 476	26 026.6	33.51	1.8	564.4
152 268	25 833.5	32.92	0	616.2

The simulation time for one FSI case based on two consecutive pulsatile flow cycles varies between 8 and 24 CPU hours depending on case grid size.

3. RESULTS

For case 1, the effects of different model suppositions and boundary conditions are reported next in detail. Figures 3(a) and (b) show the variation in pressure and WSS at the aneurysm fundus

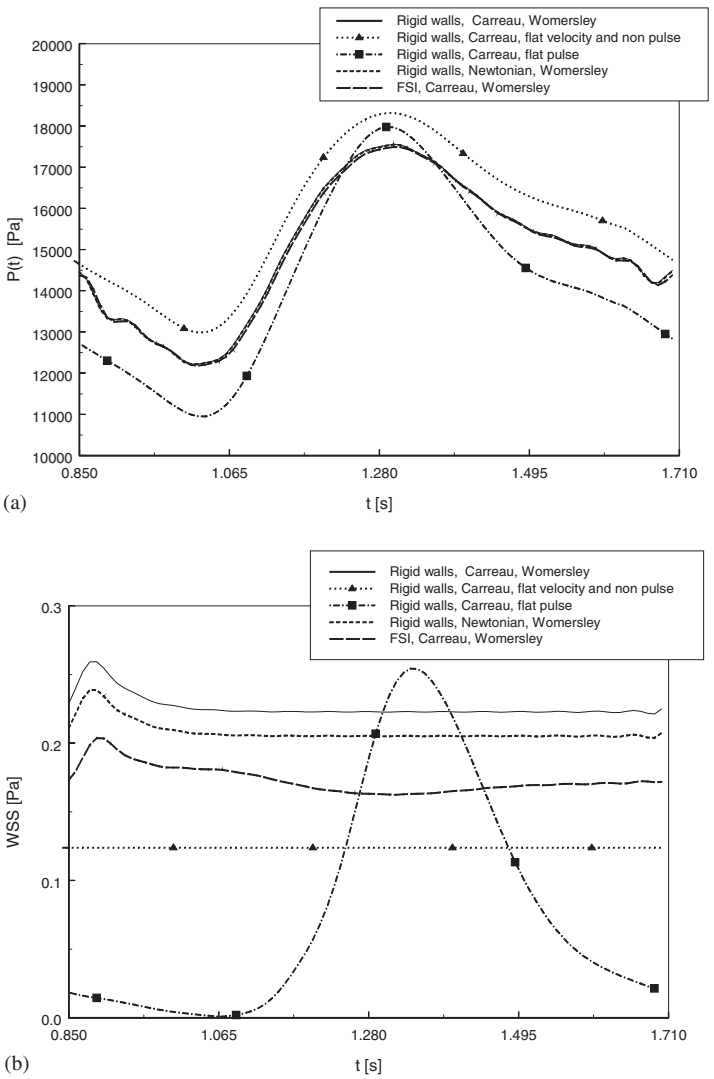

Figure 3. Variation in (a) pressure and (b) WSS with time in case 1 at the aneurysm fundus for different boundary conditions and fluid models.

with time for two fluid models and three different boundary conditions, respectively. Differences between the Newtonian and Carreau fluid model predictions on WSS and pressure are -8 and 0%, respectively, at peak systole, and it can be concluded that blood fluid model is a second-order effect in CFD of cerebral aneurysms.

As expected, the velocity inlet boundary condition has high importance for the correct prediction of fluid dynamics inside cerebral aneurysms. A steady uniform inlet mean velocity of 0.273 m/s produces differences in WSS and pressure on the aneurysm fundus of -44 and 4%, respectively, at peak systole, compared with the Womersley boundary condition, see Figures 3(a) and (b). The time variation in pressure in this case is due to the outlet boundary condition of pressure; this boundary condition was not modified. The difference in WSS prediction on the aneurysm fundus is significant and steady simulations are discarded. The effect of Womersley inlet velocity profile on variation in pressure and WSS is also important; a flat inlet velocity pulse produces differences in WSS and pressure on the aneurysm fundus of 14 and 0%, respectively, at peak systole.

For the prediction of fluid dynamics inside the aneurysm, the inclusion of FSI shows important effects in the WSS on the aneurysm fundus; the difference in prediction between CFD and CFD with FSI of WSS is 37%. It can be concluded that CFD simulations without FSI are not reliable, see Figure 3(b). Furthermore, the mechanical behavior of cerebral aneurysms under fluid dynamics loads can be obtained only with CFD considering FSI. Figures 4(a) and (b) show the time dependence of effective wall stress and wall displacement at the aneurysm fundus for different elastic Young's moduli of the wall. A reduction in the elastic Young's modulus of the wall from 2 to 1 MPa resulted in -9% lower effective stress and 77% higher displacement at the aneurysm fundus. The simulation without FSI, considering only the solid shell, can predict the wall displacement at the aneurysm fundus with 8%, but the effective stress is overestimated in 26% at peak systole; the load in this case was the pressure variation with time considered in Figure 2(b). The effective wall stress and displacement at systole are 57 290 Pa and 0.375 mm, respectively, high values that cannot be neglected, considering wall artery radius of 1.34 mm and breaking strength of a cerebral aneurysm wall ranging between 0.73 and 1.9 MPa [2].

In case 1, the pressure is nearly constant and the WSS on the aneurysm showing values lower than 3 Pa, see Figures 5(a) and (b). In case 1, the aneurysm is displaced with respect to the main artery; this characteristic produces these distributions. The maximum values of effective wall stress and displacement are located in the aneurysm neck and downstream of the bifurcation, respectively, see Figures 5(c) and (d). The magnitude of effective stress and displacement are 576 kPa and 0.64 mm, respectively; the location of maximum displacement depends on arterial morphology and the position of the aneurysm with respect to the main artery.

In case 7, with centered aneurysm with respect to the main artery, the intra-aneurysmal flow shows a nearly symmetric flow dynamics with a ring vortex enclosing the centerline jet represented by two vortices in Figure 6(b); this vortex structure defines a well-established stagnation zone where the jet impinges on the wall and where high wall pressure and displacement are expected. The displacement of the aneurysm with respect to the main artery in case 4 affects the intra-aneurysmal flow by yielding a single recirculation region at the center of the dome, see Figure 6(a). The jet of fluid through the neck of the aneurysm varies in size and position depending on the position of the aneurysm with respect to the parent artery. This finding is important for the endovascular treatment of cerebral aneurysms, since controlling blood flow at the inflow region is a critical step in achieving permanent occlusion of an aneurysm. The long-term anatomical durability of coil embolization in cerebral aneurysms by means of microcoil technology depends on the aneurysm shape and the blood flow dynamics at the aneurysm neck.

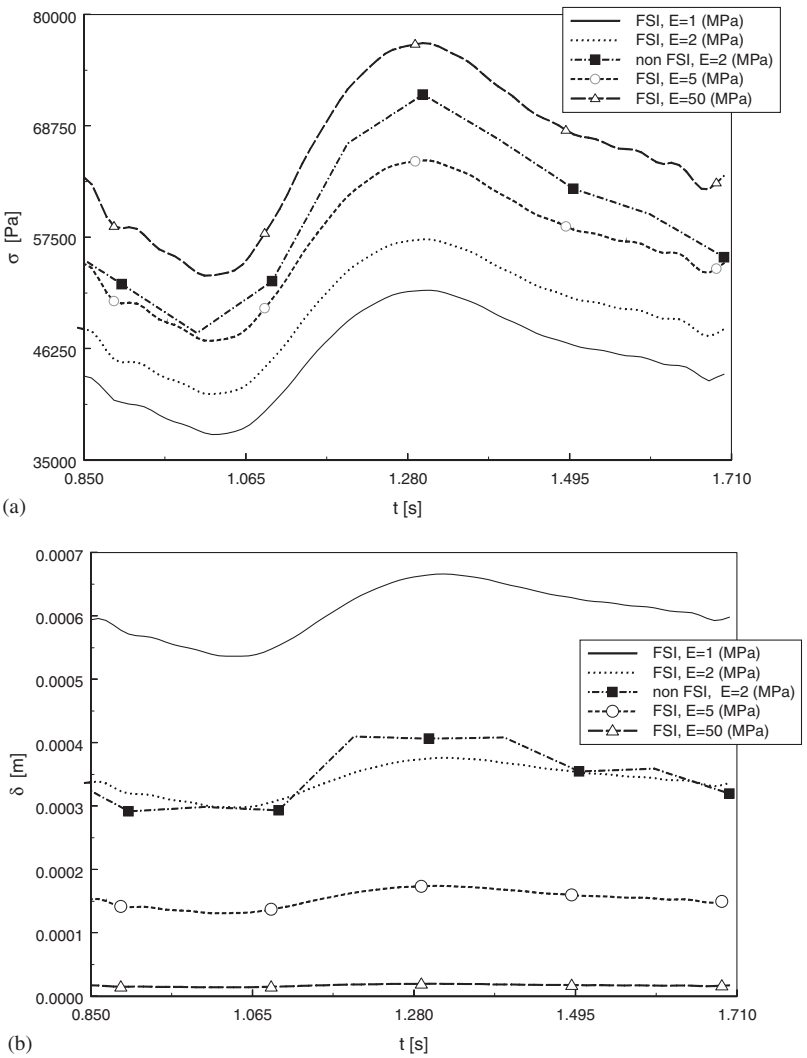

Figure 4. (a) Variation in (a) effective stress and (b) displacement magnitude with time in case 1 at the aneurysm fundus for different FSI conditions.

The temporal variation in WSS at the aneurysm fundus is an important variable for obtaining information on the cause of aneurysm wall rupture in this sensitive region. Figure 7 shows the variation in WSS for cases $2-7$. The cases with centered aneurysm with respect to the parent artery, cases 2, 3 and 7, show large WSS and values similar to those found in normal arterial flow, (WSS$\sim$6 Pa). The values of WSS are low in the cases with non-centered bifurcating aneurysms with respect to the main artery, cases $1, 4, 5$ and 6, see also Figure 3(b). Using the criterion that relates low WSS on the aneurysm fundus with bleeding risk [5], cases $1, 4, 5$ and 6 would have higher rupture risk.

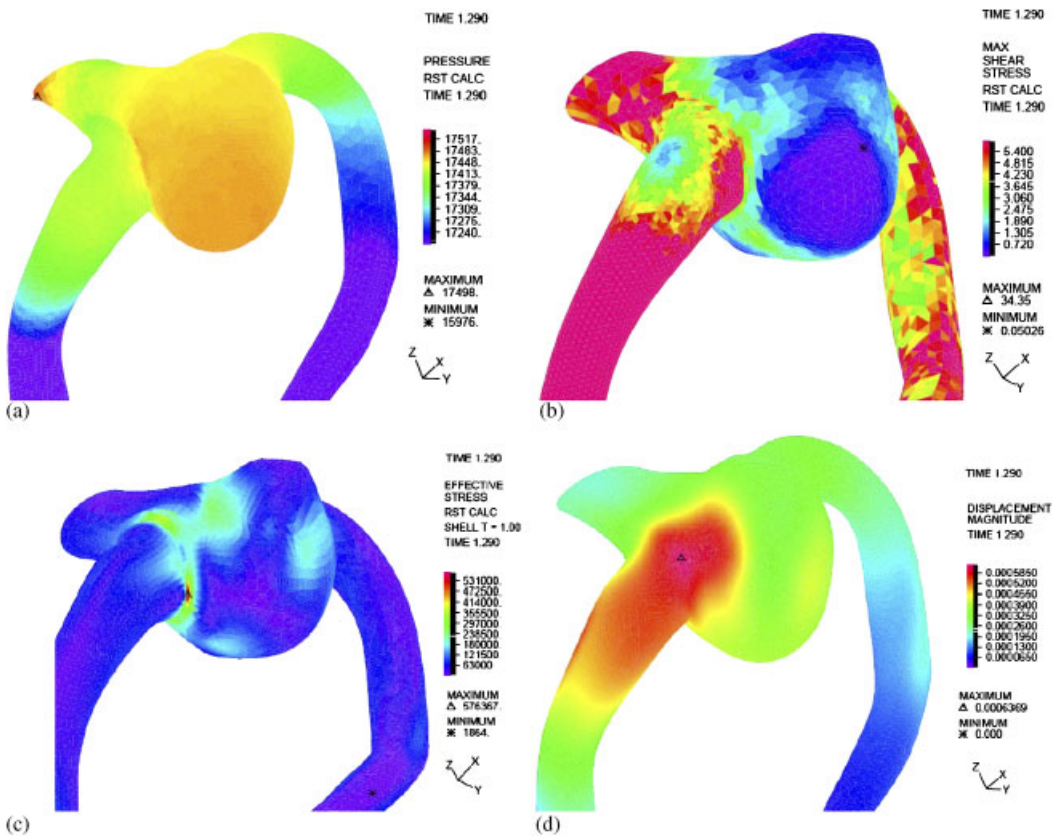

Figure 5. (a) Pressure distribution (Pa), (b) WSS distribution (Pa), (c) effective stress distribution (Pa), and (d) displacement magnitude distribution (m) contours showed for case 1 at systolic time.

Figures 8 and 9 show the effective stress and displacement magnitude distributions at peak systole in three unruptured aneurysms, cases 2, 4 and 6, and in three cases with a previous rupture of the aneurysm sac, cases 3, 5 and 7. In all cases, the maximum effective stress is located at the aneurysm neck and it reaches 614 kPa in case 3. The location of maximum displacement magnitude depends on the aneurysm position with respect to the main artery, and in case 3, it reaches 1 mm. In case 2, the aneurysm is in an early formation stage; therefore, this case cannot be directly compared with the others. In the three non-centered aneurysms with respect to the main artery, cases $4-6$, the maximum displacements are located in the wall region near the aneurysm inflow. In cases 3 and 7 with centered aneurysms, with respect to the main artery, the maximum displacements are located in the wall region where the jet impinges on the wall.

The time-averaged WSS, effective stress and displacement magnitude at the aneurysm fundus for the seven cases are showed in Table III as a function of the aneurysm surface index R_1 [13]. The values for case 2 ($R_1 = 2.7$) can be considered as a reference for bifurcating aneurysm growth due to the small aneurysm size. Considering the effective stress at the aneurysm fundus, a quadratic polynomial dependence of σ with R_1 can be observed.

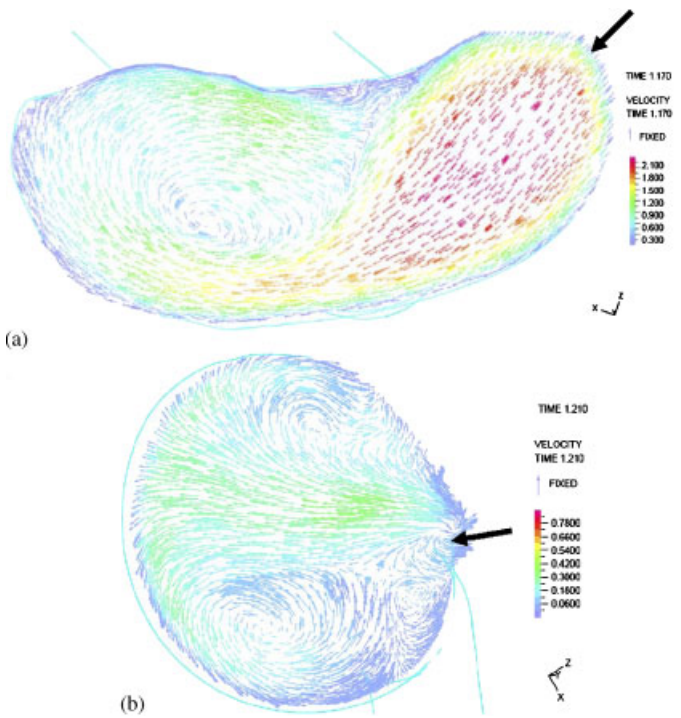

Figure 6. Velocity vectors inside the (a) unruptured cerebral aneurysm case 6 (m/s) and (b) ruptured cerebral aneurysm case 7 (m/s).

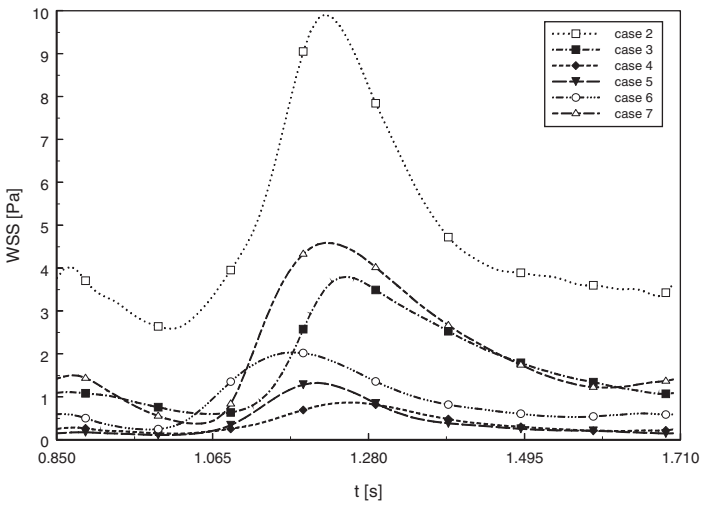

Figure 7. Variation in WSS with time at the cerebral aneurysm fundus for the seven cases.

DOI: 10.1002/fld

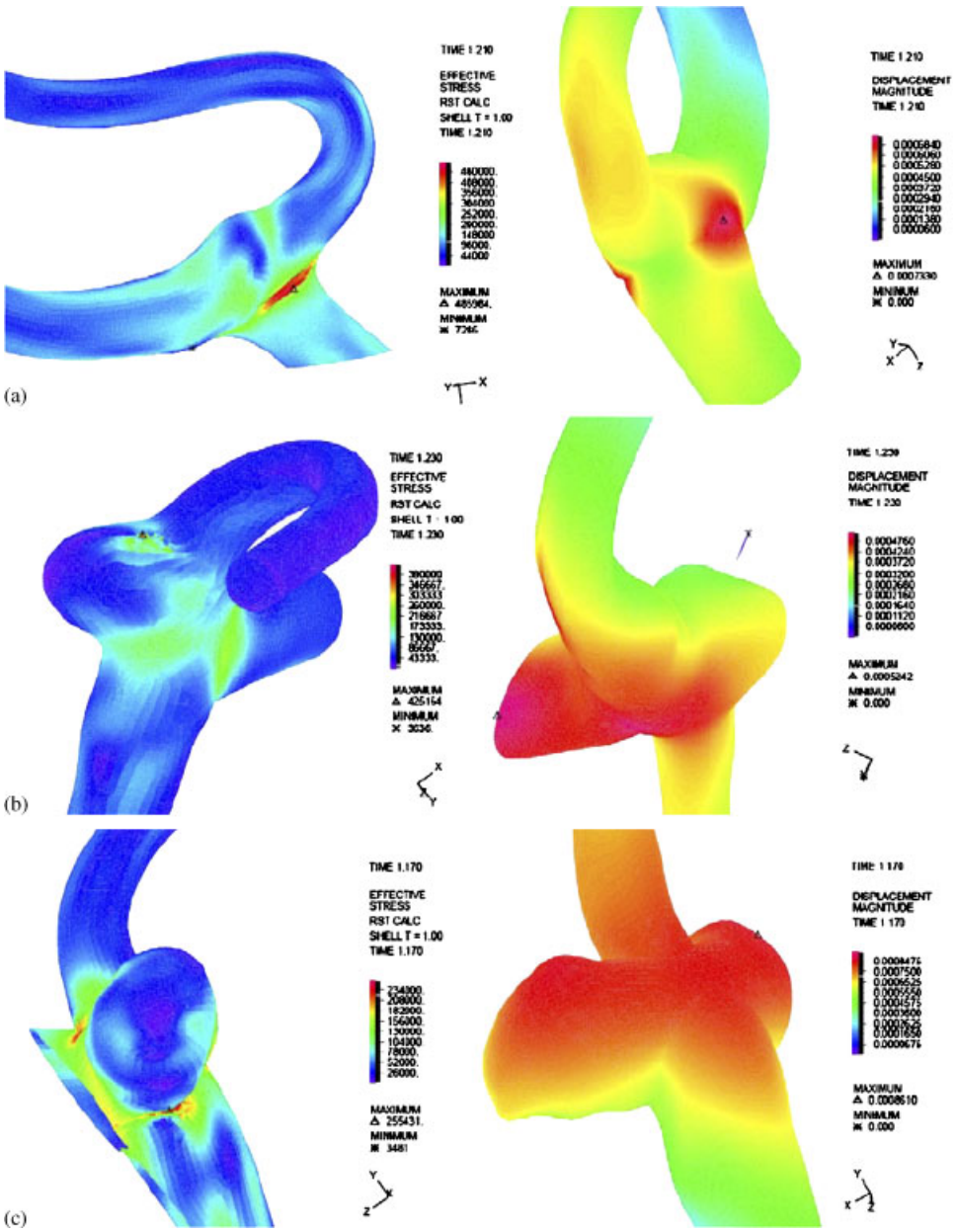

Figure 8. Effective stress (Pa), displacement magnitude (m) and distributions for unruptured cerebral aneurysms at systolic time: (a) case 2; (b) case 4; and (c) case 6.

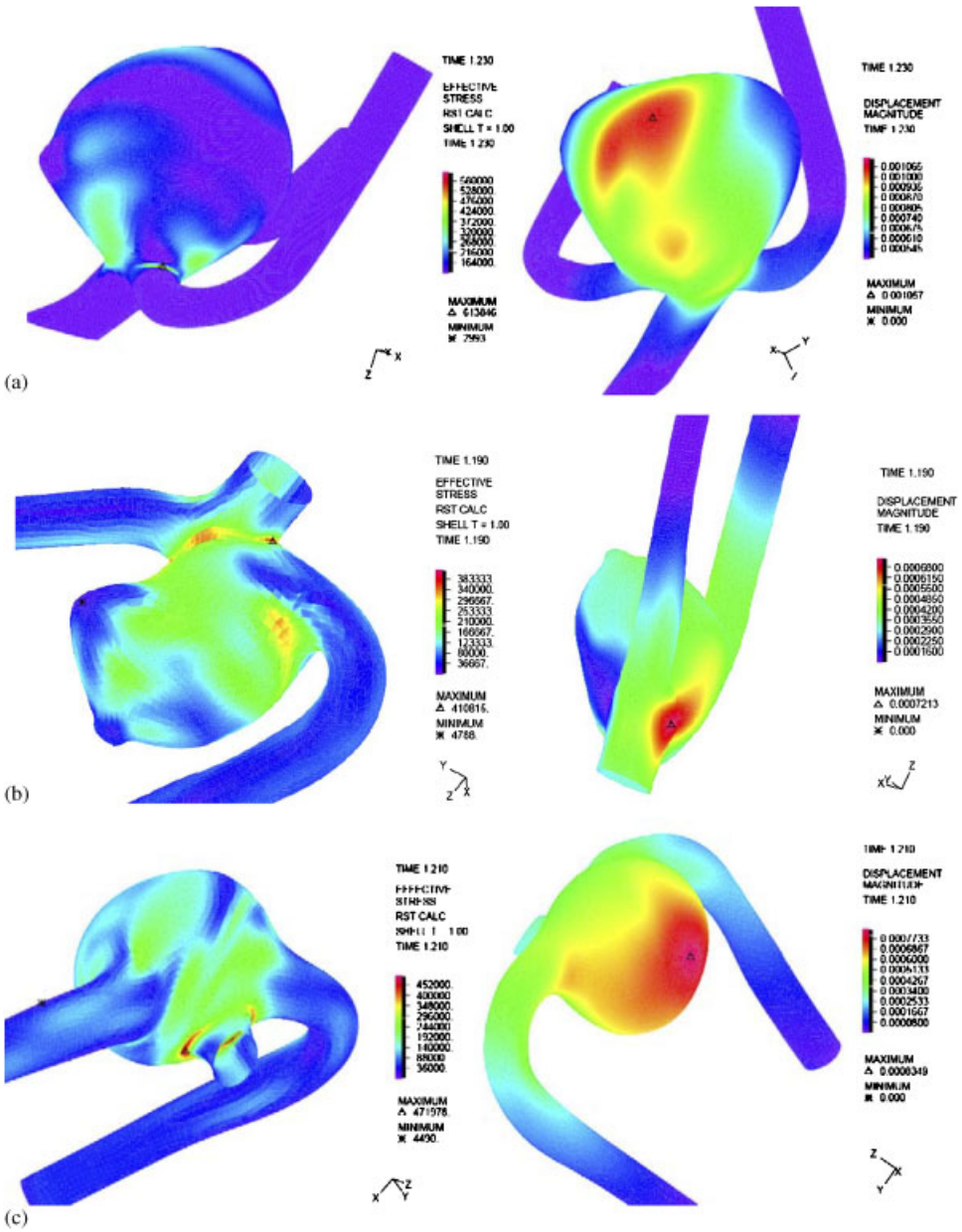

Figure 9. Effective stress (Pa), displacement magnitude (m) and distributions for ruptured cerebral aneurysms at systolic time: (a) case 3; (b) case 5; and (c) case 7.

Table III. Time-averaged WSS, effective stress σ and displacement magnitude δ at the aneurysm fundus for the seven cases.

R_1	WSS (Pa)	σ (kPa)	δ (mm)	Characteristic
2.7	4.86	126.7	0.16	U, C
3.1	0.93	4.35	0.47	U, non-C
4.5	0.39	4.59	0.28	U, non-C
11.4	0.17	50.08	0.34	R, non-C
18.7	0.44	22.47	0.28	R, non-C
40.5	1.75	157.1	0.45	R, C
42.1	2.07	170.2	0.74	R,C

R, ruptured; U, unruptured; C, centered.

4. DISCUSSION

One of the mechanisms associated with aneurysm rupture is the response of the aneurysm wall to low WSS, and it can be understood only when biological and mechanical factors are considered. Low WSS acting in regions of the aneurysms sac has been suggested as a direct cause of aneurysm rupture [5]. The biological response triggered by low WSS causes endothelial cell degeneration via apoptosis. Pentimalli *et al.* [7] have observed significant differences in apoptosis when comparing ruptured and unruptured aneurysms. High levels of apoptosis were found in 88% of ruptured aneurysms and in only 10% of unruptured lesions. We have found large regions of the aneurysm surface with low WSS (Figures 5 and 7), and these regions were larger in non-centered than in centered bifurcating aneurysms with respect to the main artery. Using this criterion, cases 1, 4–6 would have higher rupture risk. If the cell apoptosis is the controlling mechanism for aneurism wall degeneration, exclusive CFD simulations are sufficient to detect regions with low WSS and estimate rupture risk.

CFD with FSI simulations using medical image-based anatomical vascular geometries have the inherent difficulty of irregular arteries with branches of different sizes and without symmetrical characteristics. In addition, the reconstruction methodology produces small areas with high curvature. All these characteristics produce extremely high effective stress in the region of the aneurysm neck (Figures 8 and 9). However, the areas with extremely high stress are very small and are also located far from the aneurysm fundus; therefore, this high local stress does not have an important effect on stress distribution at the aneurysm surface presented in the present investigation. With the application of smoothing options implemented in Rhinoceros on bifurcations and at the aneurysm neck, the surface curvature can be reduced in these regions [13]; however, the FSI simulation produces high grid distortion in these regions and the process diverges. For this reason, the FSI simulations were performed with geometries including the simplification of high surface curvature.

Using idealized spherical aneurysm solid models and a hyperelastic model to describe the nonlinear behavior of the wall, it was found that aneurysms are dynamically stable against disturbances [28]. They used a Fung-type model to describe the pseudostrain-energy function. They found that maximum biaxial stress and strain are located at the aneurysm fundus and that maximum stress increases markedly with aneurysm size, the ratio of neck diameter to aneurysm height and pressure. Recently, Ma *et al.* [29] reported anisotropic stress analysis in patient-specific cerebral aneurysms; they used the Fung model adjusted with the experimental data of Seshaiyer *et al.* [21]. The spatial maximum of stress ranged from 0.3 MPa in small aneurysms to 1.06 MPa in a

giant aneurysm. Figures 8 and 9 reported that the maximal value of stress at the aneurysm fundus at peak systole is 0.2 MPa in case 7. The present results also show that the effective stress and displacement at the fundus increase with aneurysm size (see Table III). The minimal breaking strength in a cerebral aneurysm wall is estimated to be 0.73 MPa [2].

The experimental determination of breaking strength in representative number of cases, the analytical description of the hyperelastic behavior and the relationship between the mechanical properties and the histology in human cerebral aneurysms are needed to conclude about the dominant rupture mechanism. Considering periodic load cycle, also material fatigue can play a key role in aneurysm rupture, especially if the arterial wall is thinning via cell degeneration. This hypothesis about aneurysm rupture mechanism should be investigated in detail in the future.

5. CONCLUSIONS

This work presents numerical investigations involving hemodynamics and FSI in seven patient-specific models of bifurcating cerebral aneurysms reconstructed from 3D rotational angiography, including three unruptured and four ruptured aneurysms. In one case, the effects of different model suppositions and boundary conditions were reported in detail; the influence of the Newtonian fluid model on WSS and pressure was low; a flat steady mean velocity as inlet boundary condition produced totally different WSS and pressure at the aneurysm fundus; also with a flat pulse as inlet boundary condition, the differences in WSS and pressure were important. As expected, a reduction in the elastic Young's modulus of the artery wall resulted in lower effective stress and higher displacements at the aneurysm fundus. The simulation without FSI considering only the solid shell can predict the wall displacement at the aneurysm fundus but the effective stress is overestimated.

The WSS, the effective stress and wall displacement of the aneurysm sac showed important differences between the seven investigated aneurysms. The results strongly depend on artery and aneurysm morphology. High WSS and effective wall stress were found in the three cases with the aneurysm centered with respect to the main artery, and low values were found in the other four cases with the aneurysm displaced with respect to the main artery. Further studies are necessary to investigate the effects of arterial elasticity on the development, growth and rupture of patient-specific intracranial aneurysms in a more statistically representative number of cases.

NOMENCLATURE

A	aneurysm area
A_i	artery area at the inlet of computational domain
CFD	computational fluid dynamics
E	Young's modulus
FSI	fluid–structure interaction
f	frequency
h	artery thickness
J	Bessel function
K	Carreau model constant

p	pressure
R	artery radius
R_1	aneurysm surface index $= A/A_i$
Re	Reynolds number $= \rho U 2R/\mu$
U	mean velocity at the inlet
u	velocity
v_i	velocity component in the i direction
V	aneurysm volume
V_T	geometry volume
WSS	wall shear stress
3DRA	3D rotational X-ray angiography

Greek symbols

α	Womersley number $= R(\rho\omega/\mu)^{1/2}$
δ	wall displacement
$\dot{\gamma}_{ij}$	strain rate
μ	fluid viscosity
ρ	density
σ	stress tensor
τ	shear stress
Δt	time step
ω	angular frequency

ACKNOWLEDGEMENTS

The financial support received from FONDECYT Chile under grant number 1070773 is recognized and appreciated.

REFERENCES

1. Schievink WI. Intracranial aneurysms. *The New England Journal of Medicine* 1997; **336**:28–40.
2. MacDonald DJ, Finlay HM, Canham PB. Directional wall strength in saccular brain aneurysms from polarized light microscopy. *Annals of Biomedical Engineering* 2000; **28**:533–542.
3. Hsiai TK, Cho SK, Honda HM, Hama S, Navab M, Demer LL, Ho CM. Endothelial cell dynamics under pulsating flows: significance of high versus low shear stress slew rates ($\partial\tau/\partial t$). *Annals of Biomedical Engineering* 2002; **30**:646–656.
4. Chatziprodromou I, Tricoli A, Poulikakos D, Ventikos Y. Haemodynamics and wall remodelling of a growing cerebral aneurysm: a computational model. *Journal of Biomechanics* 2007; **40**:412–426.
5. Shojima M, Oshima M, Takagi K, Torii R, Hayakawa M, Katada K, Morita A, Kirino T. Magnitude and role of wall shear stress on cerebral aneurysm computational fluid dynamic study of 20 middle cerebral artery aneurysms. *Stroke* 2004; **35**:2500–2505.
6. Utter B, Rossmann JS. Numerical simulation of saccular aneurysm hemodynamics: influence of morphology on rupture risk. *Journal of Biomechanics* 2007; **40**:2716–2722.
7. Pentimalli L, Modesti A, Vignati A, Marchese E, Albanese A, Di Rocco F, Coletti A, Di Nardo P, Fantini C, Tirpakova B, Maira G. Role of apoptosis in intracranial aneurysm rupture. *Journal of Neurosurgery* 2004; **101**:1018–1025.
8. Steinman DA, Milner JS, Norley CJ, Lownie SP, Holdsworth DW. Image-based computational simulation of flow dynamics in a giant intracranial aneurysm. *American Journal of Neuroradiology* 2003; **24**:559–566.

9. Cebral JR, Castro MA, Burgess JE, Pergolizzi RS, Sheridan MJ, Putman ChM. Characterization of cerebral aneurysms for assessing risk of rupture by using patient-specific computational hemodynamics models. *American Journal of Neuroradiology* 2005; **26**:2550–2559.
10. Cebral JR, Castro MA, Appanaboyina S, Putman ChM, Millan D, Frangi AF. Efficient pipeline for image-based patient-specific analysis of cerebral aneurysm hemodynamics: technique and sensitivity. *IEEE Transactions on Medical Imaging* 2005; **24**:457–467.
11. Hassan T, Timofeev EV, Saito T, Shimizu H, Ezura M, Matsumoto Y, Takayama K, Tominaga T, Takahashi A. A proposed parent vessel geometry-based categorization of saccular intracranial aneurysms: computational flow dynamics analysis of the risk factors for lesion rupture. *Journal of Neurosurgery* 2005; **103**:662–680.
12. Ma B, Harbaugh RE, Raghavan ML. Three-dimensional geometrical characterization of cerebral aneurysms. *Annals of Biomedical Engineering* 2004; **32**:264–273.
13. Valencia A, Morales H, Rivera R, Bravo E, Galvez M. Blood flow dynamics in patient-specific cerebral aneurysm models: the relationship between wall shear stress and aneurysm area index. *Medical Engineering and Physics* 2007. DOI:10.1016/j.medengphy.2007.04.011.
14. Valencia A, Zarate A, Galvez M, Badilla L. Non-Newtonian blood flow dynamics in a right internal carotid artery with a saccular aneurysm. *International Journal for Numerical Methods in Fluids* 2006; **50**:751–764.
15. Torii R, Oshima M, Kobayashi T, Takagi K, Tezduyar T. Influence of wall elasticity in patient-specific hemodynamic simulations. *Computers and Fluids* 2007; **36**:160–168.
16. Oshima M, Torii R. Numerical evaluation of elastic models in blood flow–arterial wall interaction. *International Journal of Computational Fluid Dynamics* 2006; **20**:223–228.
17. ADINA. *Theory and Modeling Guide*, vol. I. ADINA R&D, Inc.: Watertown, MA, U.S.A., 2004.
18. Johnston BM, Johnston PR, Corney S, Kilpatrick D. Non-Newtonian blood flow in human right coronary arteries: steady state simulations. *Journal of Biomechanics* 2004; **37**:709–720.
19. Zhang H, Zhang X, Ji S, Guo Y, Ledezma G, Elabbasi N, deCougny H. Recent development of fluid–structure interaction capabilities in the ADINA system. *Computers and Structures* 2003; **81**:1071–1085.
20. Humphrey JD, Canham PB. Structure, mechanical properties, and mechanics of intracranial saccular aneurysms. *Journal of Elasticity* 2000; **61**:49–81.
21. Seshaiyer P, Hsu FPK, Shah AD, Kyriacou SK, Humphrey JD. Multiaxial mechanical behavior of human saccular aneurysms. *Computer Methods in Biomechanics and Biomedical Engineering* 2001; **4**:281–289.
22. Alastruey J, Parker KH, Peiró J, Byrd SM, Sherwin SJ. Modelling the circle of Willis to assess the effects of anatomical variations and occlusions on cerebral flows. *Journal of Biomechanics* 2007; **40**:1794–1805.
23. Zamir M. *The Physics of Pulsatile Flow*. Springer: New York, 2000.
24. Formaggia L, Gerbeau JF, Nobile F, Quarteroni A. Numerical treatment of defective boundary conditions for the Navier–Stokes equations. *SIAM Journal on Numerical Analysis* 2002; **40**:376–401.
25. Vignon-Clementel IE, Figueroa CA, Jansen KE, Taylor ChA. Outflow boundary conditions for three-dimensional finite element modeling of blood flow and pressure in arteries. *Computer Methods in Applied Mechanics and Engineering* 2006; **195**:3776–3796.
26. Formaggia L, Gerbeau JF, Nobile F, Quarteroni A. On the coupling of 3D and 1D Navier–Stokes equations for flow problems in compliant vessels. *Computer Methods in Applied Mechanics and Engineering* 2001; **191**:561–582.
27. Olufsen M. Structured tree outflow condition for blood flow in larger systemic arteries. *American Journal of Physiology* 1999; **276**:H257–H268.
28. Kyriacou S, Humphrey J. Influence of size, shape and properties on the mechanics of axisymmetric saccular aneurysms. *Journal of Biomechanics* 1996; **29**:1015–1022.
29. Ma B, Lu J, Harbaugh R, Raghavan M. Nonlinear anisotropic stress analysis of anatomically realistic cerebral aneurysms. *Journal of Biomechanical Engineering* 2007; **129**:88–96.